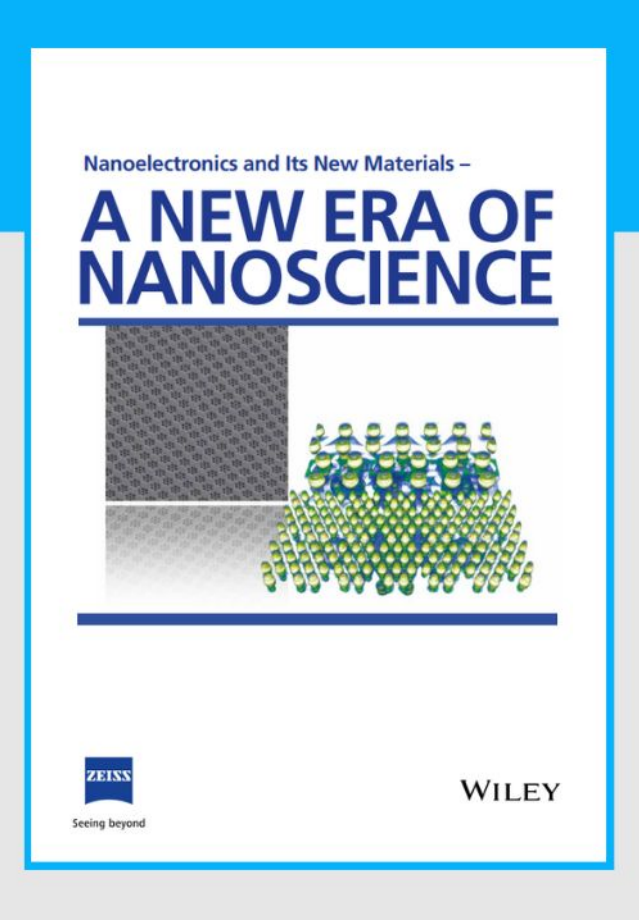


Nanoelectronics and Its New Materials – A NEW ERA OF NANOSCIENCE



Discover the recent advances in electronics research and fundamental nanoscience.

Nanotechnology has become the driving force behind breakthroughs in engineering, materials science, physics, chemistry, and biological sciences. In this compendium, we delve into a wide range of novel applications that highlight recent advances in electronics research and fundamental nanoscience. From surface analysis and defect detection to tailored optical functionality and transparent nanowire electrodes, this eBook covers key topics that will revolutionize the future of electronics.

To get your hands on this valuable resource and unleash the power of nanotechnology, simply download the eBook now. Stay ahead of the curve and embrace the future of electronics with nanoscience as your guide.



Seeing beyond



Check for updates

www.afm-journal.de

Additive Manufacturing of Porous Biominerals

Ran Zhao, Nina Kølln Wittig, Gaia De Angelis, Tianyu Yuan, Matteo Hirsch, Henrik Birkedal.* and Esther Amstad*

Nature fabricates hard functional materials from soft organic scaffolds that are mineralized. To enable an energy-efficient locomotion of these creatures while maintaining their structural stability, nature often renders parts of these minerals porous. Unfortunately, methods to produce synthetic minerals with a similar degree of control over their multi length scale porous structure remain elusive. This level of control, however, would be required to design lightweight yet robust biominerals. Here, a room temperature process is presented that combines a localized mineralization with emulsion-based 3D printing to form cm sized biominerals possessing pores whose diameters range from the 100 s of nm up to the mm length scale. The samples encompass up to 80 wt% of CaCO₃ and display a specific compressive strength that is significantly higher than that of previously reported 3D printed porous biominerals and close to those of trabecular bones. The universality of this approach by forming different types of bioactive minerals, including calcite, aragonite, and brushite is demonstrated. The ability to 3D print these materials under benign conditions renders this energy-efficient process well-suited to construct cm-sized lightweight yet load-bearing structures that might find applications, for example, in the design of the next generation of flying or motile objects.

1. Introduction

Nature fabricates lightweight, porous biominerals, such as sponges, trabecular bones, and echinoderm skeletons, that display a fascinating combination of mechanical rigidity and dexterity.^[1–3] Keys to this exceptional combination of properties are the locally changing composition and the structure that is

R. Zhao, G. De Angelis, T. Yuan, M. Hirsch, E. Amstad Soft Materials Laboratory Institute of Materials École Polytechnique Fédérale de Lausanne (EPFL) Lausanne 1015, Switzerland E-mail: esther.amstad@epfl.ch N. K. Wittig, H. Birkedal Department of Chemistry, iMAT and iNANO Aarhus University Aarhus 8000, Denmark E-mail: hbirkedal@chem.au.dk

(D)

The ORCID identification number(s) for the author(s) of this article can be found under https://doi.org/10.1002/adfm.202300950

© 2023 The Authors. Advanced Functional Materials published by Wiley-VCH GmbH. This is an open access article under the terms of the Creative Commons Attribution License, which permits use, distribution and reproduction in any medium, provided the original work is properly cited.

DOI: 10.1002/adfm.202300950

well-defined across several length scales.[4-6] Different strategies including phase separation,^[7,8] ice-templating^[9,10] and field-assisted assembly[11-13] have been applied to mimic certain aspects of the micrometer length scale structures of natural materials. Nevertheless, it is still challenging to achieve a similar multilength scales structural control as nature has so that synthetic compounds are, in most cases, mechanically weaker compared to natural materials with a similar composition, especially if normalized by their density.[14,15]

Biomineralization can be used as a bottom-up strategy to strengthen ductile polymeric scaffolds by growing minerals in them.^[16,17] However, this strategy renders the controlled incorporation of pores whose diameters span many orders of magnitudes difficult. In fact, these synthetic mineral-based composites are either thin films^[18-20] or bulk materials^[21,22] whose densities are too high for their use in locomotive applications. Even more

limiting is the short diffusion length of ions within the scaffold that restricts the dimensions of bulk composites that can be homogeneously mineralized.^[23]

Traditional ceramics with well-defined pores and a relatively high strength can be fabricated from bioinert components such as SiO_2 , $\mathrm{Al_2O_3}$, or TiO_2 . They can be made from sacrificial templates for example using inorganic precursors, [24] solgel chemistry, [25] or nanoparticle-stabilized emulsions, so-called Pickering emulsions. [26] The rheological properties of some of these formulations can be adjusted to enable 3D printing. [27,28] However, a supportive gel matrix or a post heat-treatment is usually needed to strengthen the printed structures. [29-32] Unfortunately, the post-processing step is energy-consuming, especially if sintering is involved, and prevents the use of temperature-sensitive components. It also typically compromises the shape fidelity of the materials as it involves significant shrinkage of the printed parts. [7,24,30,33]

Here, we introduce an emulsion-templated water-based biomineralization process that offers a unique control over the size of pores from the 100 s of nm up to the mm length scale. Oil-in-water emulsions are stabilized with pyrogallol-functionalized surfactants that can be ionically crosslinked with metal ions like Ca²⁺ or Fe³⁺ to convert the emulsions into viscoelastic capsules.^[34–36] These capsules are up-concentrated to form a shear-thinning ink that can be 3D printed into cm-sized

www.afm-journal.de

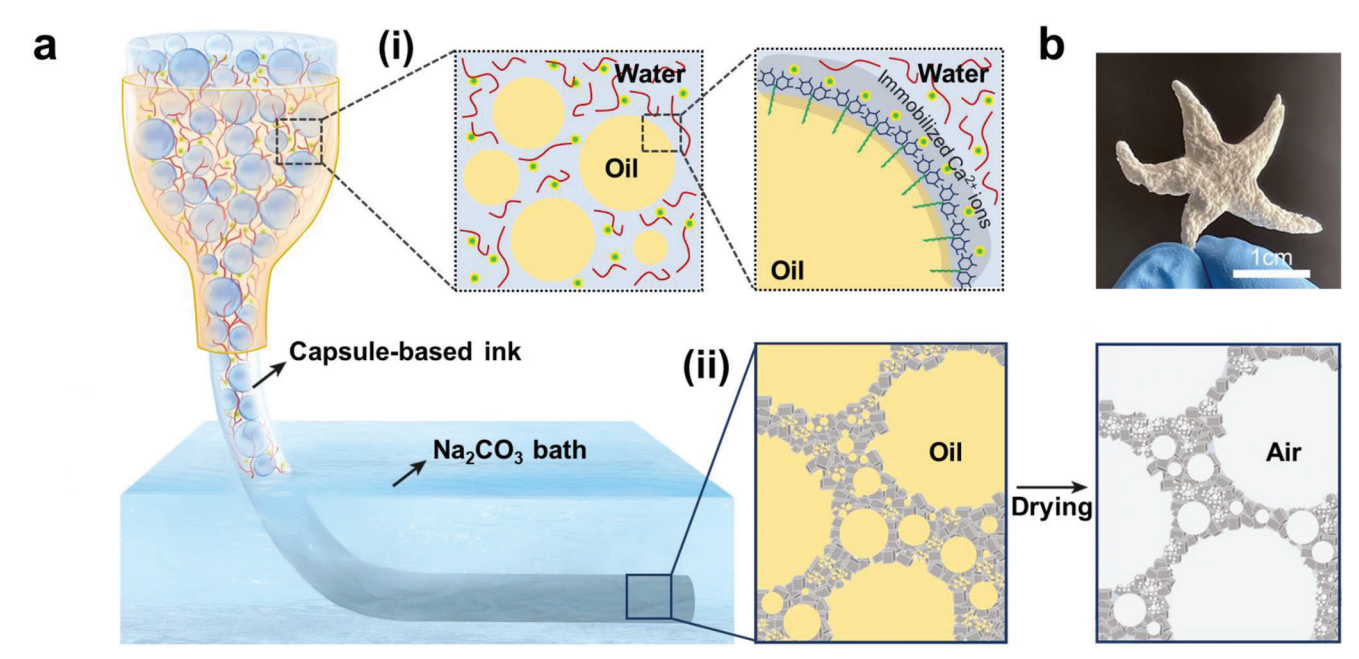


Figure 1. 3D printing of porous mineral-based composites. a) Schematic illustration of the fabrication of porous $CaCO_3$ composites by combining 3D printing of emulsions with localized biomineralization. (i), Ink formulation and processing. The ink is composed of oil-in-water emulsions that are stabilized with functionalized block-copolymer surfactants ($\stackrel{\leftarrow}{\leftarrow}$) which can selectively bind certain cations such as Ca^{2+} ions ($\stackrel{\bullet}{\circ}$). These capsules are dispersed in an aqueous solution containing poly(vinyl alcohol) (PVA) ($\stackrel{\leftarrow}{\smile}$) and up-concentrated to form a 3D printable ink. (ii), The resulting structures are rigidified through mineralization. Upon addition of CO_3^{2-} , the minerals preferentially precipitate at the capsule surface, forming a thin mineral shell. The objects are dried in air resulting in porous structures. b) Photograph of a cm-sized 3D printed porous starfish.

structures possessing well-defined shapes. If printed into a carbonate-containing aqueous solution, the capsule surfaces mineralize, resulting in structures possessing pore sizes that are determined by the size of the emulsion drops they are made from, as shown in **Figure 1** and Movie S1 (Supporting Information). Importantly our process can be conducted in aqueous media at room temperature, thereby consuming minimum amounts of energy. Nevertheless, it results in composites comprising up to 80 wt% CaCO₃ that display a stiffness, hardness, and specific compressive strength similar to values of human trabecular bone. We envisage this material to open up new possibilities to regenerate porous biominerals or to serve as a lightweight material to build rigid, yet agile motile objects.

2. Results and Discussions

Nature produces porous minerals possessing architectures that are well-defined from the nm up to the mm length scale. [37] To control the pore size and size distribution of our synthetic biominerals over a similar range as nature does, we combine an in situ mineralization process with emulsion-based 3D printing. The size of small pores, with diameters ranging from the 100 s of nm up to the 100 s of μ m, is tuned with emulsion templates. Emulsion drops with diameters between 200 nm and 120 μ m are prepared by mixing a fluorinated oil, HFE7500, with an aqueous solution containing calcium chloride (CaCl₂) and poly(vinyl alcohol) (PVA). To prevent coalescence of the emulsions, we add an amphiphilic block copolymer surfactant whose hydrophilic block is end-functionalized with two pyrogallols to the oil phase, [38,39] as schematically shown in Figure S1 (Supporting Information).

The oil/water mixture is tip sonicated for 6 min to result in polydisperse oil-in-water drops whose diameters are hundreds of nanometers. The end-functionalized surfactants adsorb at the drop surface where they are crosslinked by calcium ions (Ca²⁺) contained in the aqueous phase to transform drops into capsules.

To enlarge the range of drop sizes we can produce, which directly translates into the range of pore sizes that can be introduced into our biominerals, we fabricate emulsion drops by vortexing the oil/water mixture for 25 s. The resulting drops are again polydisperse, yet their diameters are significantly larger, they range from 6 to 52 µm and average at 22 µm with a standard deviation of 12 µm. Drops with a narrower size distribution are fabricated with microfluidic flow-focusing devices by injecting the inner oil phase containing the surfactant at a flow rate of 30 µL min⁻¹ and the outer aqueous phase containing Ca²⁺ and PVA at a flow rate of 50 µL min⁻¹. The resulting drops display an average diameter of 112 µm and a standard deviation of 8 µm. as illustrated in the optical micrographs in Figure S2 (Supporting Information) and summarized with the diameter distributions in Figure S8 (Supporting Information). Note that these emulsions remain stable for at least 3 d, which is much longer than the duration of our experiments, as shown in Figure S3 (Supporting Information).

To control the structure of porous materials on larger length scales, we 3D print the emulsion templates. To convert emulsions into 3D printable inks, we up-concentrate the drops through sedimentation. Thereby, emulsions closely pack such that they experience friction when sliding past their neighbors; this feature introduces a shear thinning behavior to the ink that is crucial for extrusion-based 3D printing. [40] Indeed, the resulting ink

conditions) on Wiley Online Library for rules of use; OA articles are governed by the applicable Creative Commons



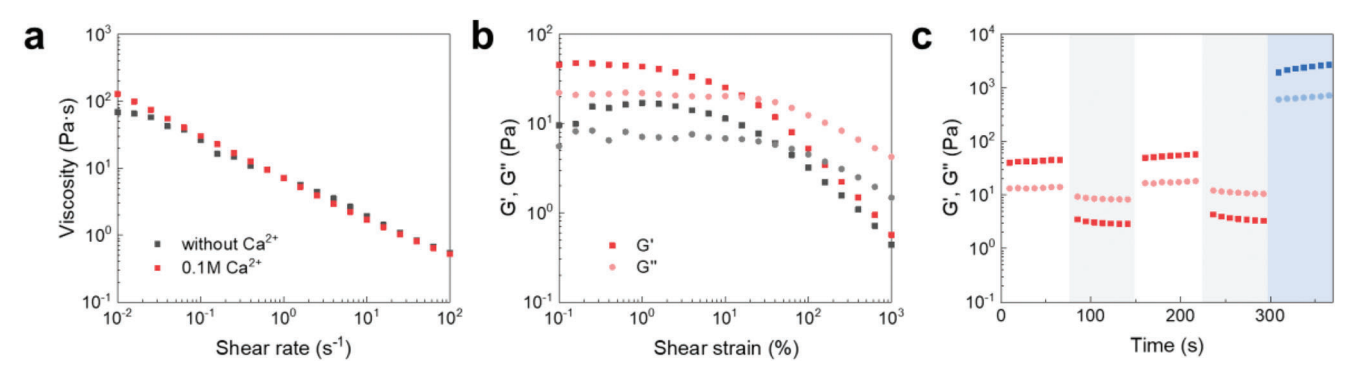


Figure 2. Rheology of the capsule-based inks. a) Flow and b) amplitude sweeps of inks composed of up-concentrated emulsions in the presence of 0.1 m Ca^{2+} (red) and in the absence of crosslinking ions (black). c) Oscillatory strain relaxation measurements of the capsule-based inks in the presence of 0.1 m Ca^{2+} tested by cycling the ink between 1% (white background) and 100% strain (gray shaded area). At t = 300 s, the ink is immersed into an aqueous solution that is saturated with Na_2CO_3 where it turns into a gel (blue symbols in blue shaded area).

shear-thins, independent of the Ca^{2+} and PVA concentrations present in the aqueous phase, as shown in **Figure 2a** and Figure S4 (Supporting Information). By contrast, the viscosity and the flow point, defined as the crossover of the storage (G') and loss modulus (G'') in oscillation amplitude sweep measurements are influenced by the Ca^{2+} concentration. For example, inks containing 0.1 M Ca^{2+} possess an increased viscosity and lower strain at the flow point compared to those lacking any Ca^{2+} ions, as summarized in Figure 2b. We assign the difference in viscosity to the increase in inter-capsule interactions that come from the rougher surfaces of ionically crosslinked capsules and the inter-capsule crosslinking via Ca^{2+} ions. [41] The enhanced interactions among capsules composed of ionically crosslinked surfactants also condense the ink formulation and hence, decrease the strain at the flow point of the ink.

To ensure a good shape fidelity of the 3D printed parts, the ink must rapidly recover its storage modulus once the shear is released. To demonstrate this feature, we perform shear recovery tests on our samples by repetitively shearing them for 60 s at 1% strain followed by 60 s of shear at 100% strain while recording the storage and loss moduli. Indeed, the ink displays rapid, reversible transitions from solid-like to liquid-like states, as shown during the first 300 s in Figure 2c.

The storage modulus of our viscoelastic ink is too low to ensure good shape retention of 3D printed parts. To overcome this limitation, we print our ink into an aqueous bath containing $\mathrm{Na_2CO_3}$ to initiate the gelation of $\mathrm{PVA}^{[42]}$ and the mineralization of the capsule surfaces. Indeed, upon insertion into the carbonate source, the storage modulus of the printed filaments increases instantly to 2000 Pa; this value is 400 times higher than that of the original ink, as shown in the blue shaded area in Figure 2c. We assign the abrupt increase in storage modulus primarily to the precipitation of PVA, that is caused by its lower solubility in salt-rich aqueous solutions, according to the Hofmeister effect. [43]

To transform a capsule-based ink into a solid porous structure, we must selectively induce mineralization at the capsule surfaces and in the surrounding aqueous solution. Our capsules present pyrogallol functionalities at their surfaces pointing towards the aqueous phase , as schematically shown in Figure 1a. Hence, the surfactants endow the capsule surface a high affinity towards Ca^{2+} owing to the Ca^{2+} –pyrogallol interactions. $^{[44]}$

Previous reports demonstrated that PVA films^[45] or organic matrices containing metal-coordinate complexes^[46,47] template the growth of inorganic precipitates. Hence, we expect minerals to preferentially start to form at the capsule surface, when capsules presenting high concentrations of Ca2+ ions at their surfaces are immersed in an aqueous solution containing a carbonate source. By contrast, minerals cannot form within drops as they are composed of oil where Ca^{2+} and CO_3^{2-} ions have a very low solubility. We investigate the mineral-polymer interactions using Raman and Fourier-transform infrared (FTIR) spectroscopy. Indeed, we observe the peaks from surfactants, the PVA matrix as well as CaCO₃ crystals in Raman spectra of samples that have been mineralized, as shown in Figure S5 (Supporting Information). The O-H stretch vibration from the phenolic hydroxyl groups in the FTIR spectrum shifts from 3300-3050 cm⁻¹ to 3400-3150 cm⁻¹ upon crosslinking with Ca²⁺ and mineralization, indicating that the pyrogallols indeed interact with Ca²⁺ ions.

Mineralization that happens within a polymer matrix typically increases the storage and loss moduli of the polymer.[47] To assess if this is also the case for our mineralized materials, we perform frequency sweeps on our samples and quantify the plateau moduli as a function of the time that samples have been incubated in the mineralizing solution. Initially, the stiffness rapidly incrases. Within the first hour of incubation, the stiffness continues to increase before it plateaus, as shown in Figure S6a,b (Supporting Information). To differentiate the increase of the gel stiffness caused by its mineralization from the precipitation of PVA caused by the Hofmeister effect, we monitor the mineral content as a function of the time the ink has been incubated in a Na2CO3-containing bath. The mineral content steadily increases within the first hour of incubation and plateaus thereafter, as summarized in Figure S6c (Supporting Information). This mineralization time is much longer than the time it takes the storage modulus of our ink to increase upon contact with a CO₃²⁻-containing solution, as a comparison with Figure 2c reveals. This comparison suggests that the observed initial rapid incrase in storage modulus is mainly attributed to the precipitation of PVA. This suggestion is supported by the fact that the storage modulus of Ca²⁺-free inks, measured after 5 min of incubation in a Na₂CO₃-containing bath, is very close to that of Ca²⁺-containing



www.afm-journal.de

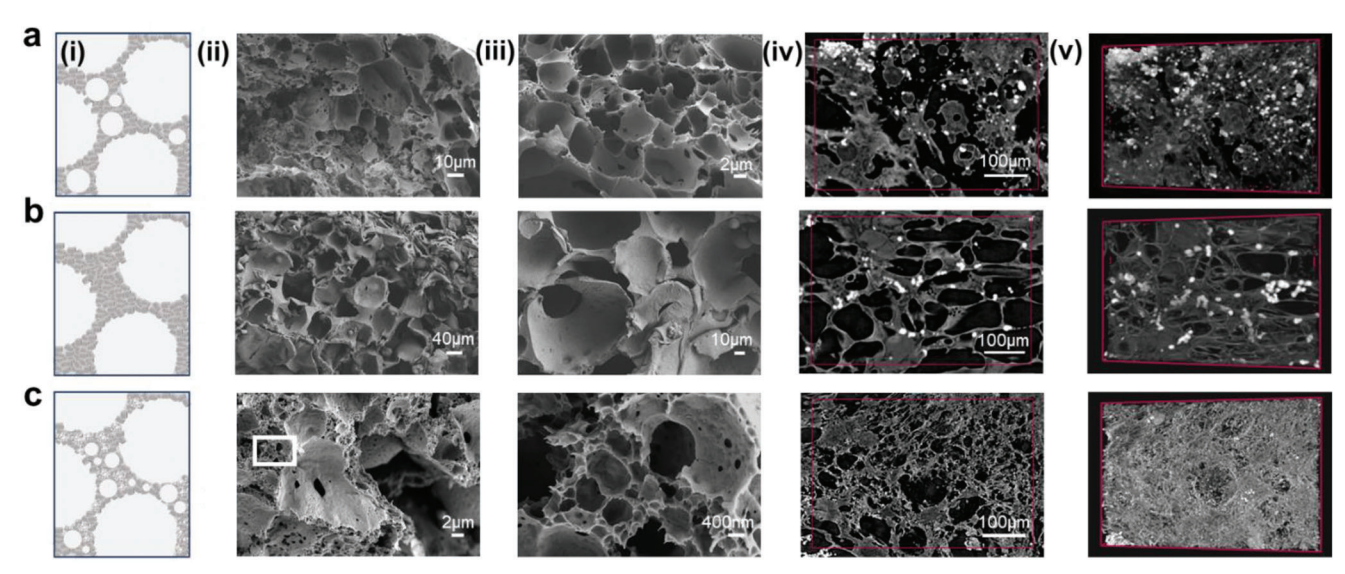


Figure 3. Microstructure of porous composites. (i) Schematic illustrations, (ii) overview and (iii) close-up SEM micrographs, (iv) tomographic slices, and (v) 3D renderings of porous minerals made from emulsions that have been formed a) through vortexing, b) using a microfluidic device and c) by mixing two batches of emulsions with different average drop sizes, one formed through tip sonication the other through vortexing. Samples are made from capsule-based inks containing 0.1 м Ca²⁺ and 5 wt% PVA. The red boxes in (iv) mark the central virtual slices of the 3D region of interest (ROI) shown in (v).

ink, as shown in Figure S6d (Supporting Information). By contrast, the storage modulus of the Ca^{2+} -free ink is significantly lower than that of the Ca^{2+} -containing one if they have been incubated in the Na_2CO_3 -containing solution for 1 h, where according to our thermogravimetry (TGA) results, most of the minerals have formed. These results confirm our hypothesis that the rapid increase in storage modulus of our ink upon contact with a CO_3^{2-} -containing solution is primarily caused by a gelation of PVA.

To test if the mineral formation is limited by the amount of Ca^{2+} present within the system, we quantify the plateau storage modulus of scaffolds that have been mineralized for 1 h as a function of the Ca^{2+} concentration initially contained in the capsule-based ink. Indeed, the plateau storage modulus of these samples increases with the Ca^{2+} concentration contained in the ink, as shown in Figure S7 (Supporting Information), indicating that the amount of Ca^{2+} in the system limits the degree of mineralization of our capsules.

A rapid solidification of the ink risks clogging of the printer nozzle, which might compromise the robustness of the process. The mineralization of the ink takes approximately 1 h. We typically print at a speed that varies between 15 and 30 mm s⁻¹, depending on the ink formulation, such that the printing of a grid with dimensions of 10 mm \times 10 mm \times 3 mm takes less than 3 min, as exemplified in the Movie S2 (Supporting Information). Because the printing time is much shorter than the mineralization time, we do not risk a mineral-induced clogging of the nozzle. To avoid any back-flow of the printing bath into the nozzle, which would risk inducing its clogging, we continuously eject the ink into the printing bath using an optimized pressure that varies between 25 and 45 kPa. As a result of these precautions, we never observe clogging of the nozzle even if we print structures continuously for 15 min, as shown in Movie S1 (Supporting Information).

To transform the mineralized structures into porous materials, we dry them in air. The fluoroether-based oil we use has a vapor pressure of 2.1 kPa at 25 °C. This value is close to that of water, which possesses a vapor pressure of 3.2 kPa at 25°C, such that the solvent evaporates at room temperature. To quantify the sizes of the resulting pores, we visualize dried samples with scanning electron microscopy (SEM). Samples made from emulsions prepared by vortexing display pore diameters ranging from 4 to 45 μm with an average of 18 μm and a standard deviation of 11 µm, as shown in Figure 3a and Movie S3 (Supporting Information). This pore diameter range is very similar to the diameter of the emulsion drop templates they have been made from, as shown in Figure S8 (Supporting Information), in good agreement with previously reported results on the fabrication of porous ceramics from emulsion templates.^[26,27] The slight decrease in pore sizes compared to the initial drop sizes can be assigned to the shrinkage of the structure caused by capillary forces. To test if this correlation also holds for larger drops, which are more difficult to stabilize against coalescence, we analyze the pore sizes of samples prepared from monodisperse emulsion drop templates. Also in this case, the correlation between drop and pore sizes is very good: these samples possess pores with an average diameter of 87 µm and a standard deviation of 17 µm, as shown in Figure 3b. These results highlight the good stability of our emulsions that do not coalesce even if subjected to shear forces during the 3D printing process, as shown in Figure S9 (Supporting Information). As a result of the good emulsion stability, the vast majority of the pores are spherical, as shown in the X-ray micro-computed tomography (μ-CT) images in Figure 3biv,v and Figure S10b (Supporting Information).

The pore architecture in porous materials strongly influences their mechanical properties.^[48,49] The best density-normalized mechanical performance is typically achieved in materials possessing a highly ordered hierarchical architecture.^[50] However,

and-conditions) on Wiley Online Library for rules of use; OA articles are governed by the applicable Creative Commons

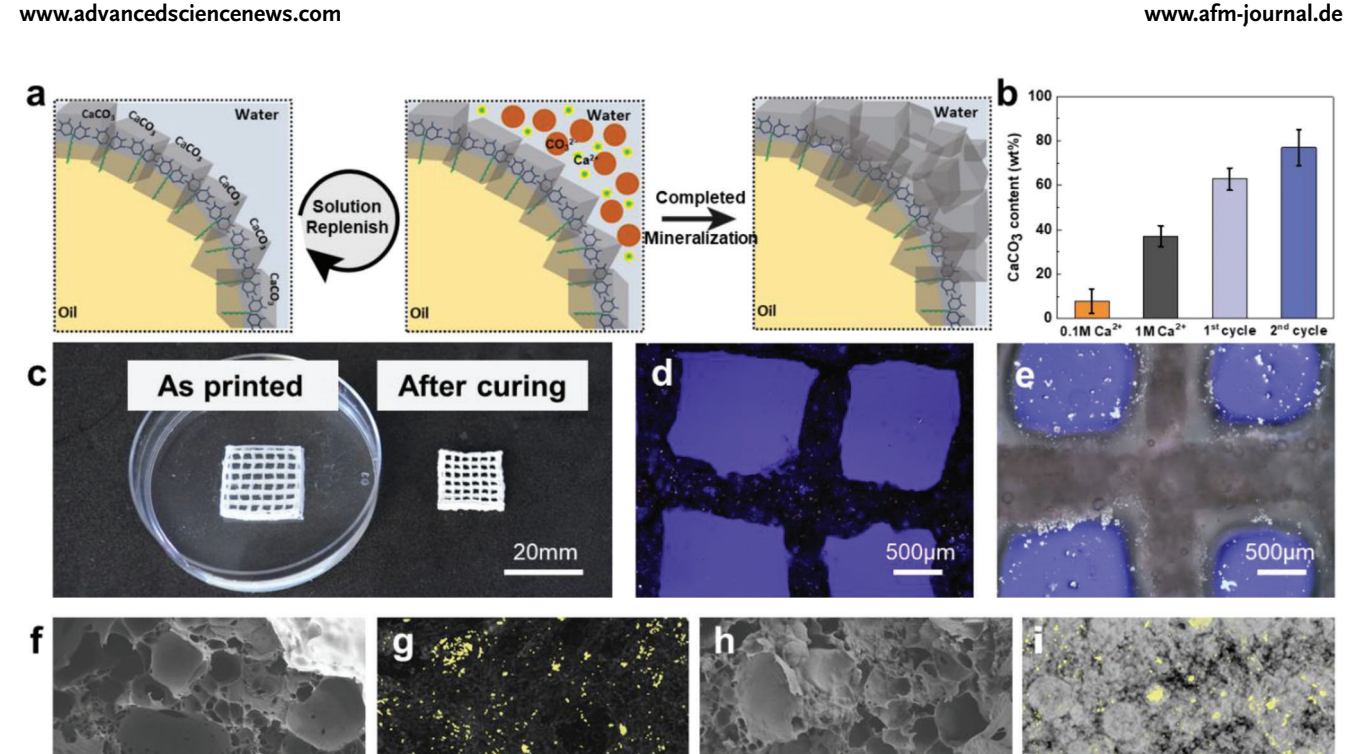


Figure 4. Curing of 3D printed structures. a) Schematic illustration of the curing of 3D printed CaCO3 minerals by repeatedly replenishing the aqueous bath solution with Ca²⁺ and a carbonate source. b) Influence of the initial Ca²⁺ concentration and the number of mineralization cycles the composite has been subjected to on the weight fraction of CaCO3 within it, as determined through thermogravimetric analysis (TGA). c) Photograph of a 20 mm × 20 mm × 3 mm printed lattice that has been subjected to two mineralization cycles. The cured grid displays a low volume shrinkage and high shape fidelity. d,e) Polarized optical microscopy images of samples d) before and e) after they have been subjected to three mineralization cycles. f,h) SEM images and g,i) 3D renderings of X-ray μ -CTs of samples f,g) that have not been subjected to any additional mineralization cycle, showing the interconnected pore structures and h,i) after having been subjected to two additional mineralization cycles, demonstrating the formation of intact spherical mineral shells. The yellow parts inside the 3D renderings mark the pores that are isolated from the sample surfaces.

processes that lead to structures with hierarchical porosities typically require high energy input, such as ice-templating, [9] pyrolysis^[24] or metal oxidation during sintering.^[51] To test if our low energy process enables the formation of structures possessing pores whose diamters span many orders of magnitudes, we mix two batches of emulsions possessing drops with different sizes: We mix one batch of emulsions produced through vortexing, whose drop diameters are in the tens of µm, with one batch produced by tip sonication, whose drop diameters are of order 100 nm. The emulsion mixture is up-concentrated, molded and mineralized before it is dried and visualized using SEM and X-ray μ -CT. Indeed, these samples contain pores with diameters ranging from 100s of nm up to 10s of µm, as exemplified in Figure 3c. Note that the pore size distribution can be conveniently turned by changing the volume ratio of the two emulsion

An important parameter that determines the shape fidelity of 3D printed parts is their shrinkage upon drying. While shrinkage can be partially avoided by drying in a humid environment, this process prolongs the drying time. To shorten the processing time and prevent that capillary forces collapse pores during drying, we strengthen our composite by enhancing the inter-particle links with additional minerals, thereby increasing the volume

fraction of minerals. This can be achieved by increasing the initial Ca²⁺ concentration in the ink to 1 м. Indeed, these structures contain pores with diameters of order 10s of µm, as exemplified in the X-ray μ-CT virtual tomography slice and 3D renderings in Figure S11a (Supporting Information). Unfortunately, the stability of the emulsion drops decreases if the Ca²⁺ concentration is increased above 1 M, and hence compromises the shape fidelity of the porous structure.

To address this limitation while still increasing the mineral fraction in the composites, we keep the Ca²⁺ concentration at 1 м and subject the 3D printed structures to repeated mineralization cycles. This is achieved by washing the 3D printed structures before immersing them in an aqueous solution containing 1 м Ca²⁺ for 2 h and again incubating them in an aqueous solution containing 1 M CO₃²⁻ for 2 h, as schematically illustrated in Figure 4a. We quantify the shrinkage of our composite by measuring the dimensions of samples as printed in the bath and after drying. Indeed, the shrinkage of the printed object linearly decreases from \approx 45% to \approx 16% with increasing number of mineralization cycles, as evidenced by direct measurements on a 20 mm × 20 mm × 3 mm printed lattice after two mineralization cycles, shown in Figure 4c and Figure S12 (Supporting Information). This degree of shrinking is much lower than that typically



www.afm-journal.de

observed during pyrolysis of polymer-derived ceramics, which is usually around 30%. [7,24]

We assign the measured reduction in shrinkage with increasing mineralization cycles to an increase in the mineral content of the composite. To test this hypothesis, we quantify the CaCO₃ weight fraction of composites that have undergone up to three mineralization cycles using TGA. The CaCO₃ content increases with mineralization cycles, with an average of 77 wt% in samples subjected to two mineralization cycles, as shown in Figure 4b. To visualize the effect of the additional mineralization on the porosity of our samples, we image them with SEM and X-ray μ-CT. Samples that have not been subjected to any mineralization cycle possess many interconnected open pores, as shown in Figure 4f,g. We assign the open porosity to a partial collapse of the structure during the evaporation of the solvent. By contrast, samples subjected to two mineralization cycles contain many spherical pores that are much less interconnected, as shown in Figure 4h,i. We assign this finding to the newly formed CaCO₃ that can only grow within the hydrophilic parts of the composites, which is the surrounding of the pores. As the mineral content increases, the interstitial spaces become increasingly mineralized, eventually leading to the formation of intact, closed, spherical mineral shells. As expected from the influence of the additional mineralization cycles on the pore structure, these additional mineralization cycles also change the surface morphology, as a comparison of SEM images of a filament taken before and after it has been subjected to two mineralization cycles shown in Figure S13 (Supporting Information) reveals.

The mineral content can only be controllably increased by subjecting the samples to multiple mineralization cycles. It cannot be increased by increasing the initial Ca²⁺ concentration as a high Ca²⁺ concentration results in a collapse of these spherical structures. However, if we subject the composite to more than two mineralization cycles, we compromise its shape fidelity because crystals start to grow out of the 3D printed filaments. For example, filaments formed by extruding the paste through a 515 µm diameter nozzle, initially have a diameter of approximately 360 µm, as shown in Figure 4d. This diameter increases to 550 µm when the filament is subjected to two mineralization cycles and to 800 µm after three mineralization cycles, as shown in Figure 4e. Based on these results, we subject our samples to two mineralization cycles as this protocol results in the best shape fidelity while still reaching a high mineral content. These results nicely demonstrate the degree of control over the microstructure and pore interconnectivity our process offers.

To assess the influence of the pore structure on the mechanical properties of our porous materials, we perform nanoindentation (NI) tests on them. To perform reproducible nanoindentation tests, we pre-press our samples and polish their surfaces to reduce the surface roughness, as detailed in the experimental section. Note that these pre-treatments typically lead to a densification of the surface, which increases the hardness and modulus of the sample. Hence, we expect the hardness and modulus values reported here to be more similar to those of nonporous bulk minerals. Indeed, nanoindentation tests, which typically require polishing of the samples, can result in higher hardness values than microindentation tests performed on unpolished samples.^[52] Yet, because we pre-treat our samples identically, we can compare hardness and modulus values between dif-

ferent samples. The hardness of our polymeric scaffold increases up to 12-fold and its stiffness up to 4.5-fold upon mineralization, as shown in **Figure 5**a and Figure S15 (Supporting Information). Indeed, samples subjected to two mineralization cycles display a hardness and stiffness similar to those of human trabecular bones, even though bulk calcite is weaker than hydroxyapatite. [53] We assign the good mechanical properties of our composites to the high mineral content.

The compressive strength of composites is closely related to their density. To perform a fair comparison between our samples, we plot the strength measured in uniaxial compression tests as a function of their density. As expected, molded bulk samples possessing pores whose diameters span many orders of magnitudes, labeled as "hierarchical pores," have lower densities than samples containing pore diameters that are all within a similar length scale, referred to as "polydisperse pores," as summarized in Figure 5b. Yet, the two types of samples display similar compressive strengths, quantified based on the stress-strain curves shown in Figure S16 (Supporting Information). We assign this finding to the stress distribution within porous composites: Composites possessing pore sizes that span many orders of magnitudes contain many small mineral struts that enable an efficient stress transfer and prevent extensive distortions and associated build-up of stress concentrations in the macro-struts.^[51,54] Nature often uses this trick to build lightweight yet damage-resistant materials such as bamboo,^[55] the skeleton of glass sponges,^[1] avian bones and feathers.^[56] Note that the density of our samples is lower than that of the most commonly studied synthetic bioceramics possessing similar compressive strengths even though these bioceramics are typically based on hydroxyapatite (HA) or β -tricalcium phosphate (β -TCP), which have higher strengths than CaCO₃ used here, [53,57] as shown in Figure 5b. This comparison shows the power of controlling the pore size over many orders of magnitudes and the potential of our method to build lightweight and strong materials.

A comparison between our samples and lightweight, damageresistant natural biominerals reveals that we have a specific strength similar to that of avian beaks and very close to trabecular bones as summarized in Figure 5c. To further reduce the density of molded samples with hierarchical pores, we leverage the 3D printability of our ink to design structures that include mm sized pores. To perform compression tests, we 3D print cubes with diameters of 10 mm \times 10 mm \times 5 mm possessing a controllable porosity ranging from the 100 nm up to the mm length scale, as shown in Figure S14 (Supporting Information). Note that even though we did not use monodisperse emulsion drop templates to fabricate these hierarchical structures, our method offers the opportunity to do so. Thereby, it would enable the design of structures possessing ordered and well-defined pores or gradients in pore sizes that possess even higher strengths and stiffnesses, as can be found, for example, in cuttlebone.^[58]

The mechanical properties of CaCO₃-based composites depend on the CaCO₃ structure, which can be tuned with appropriate additives present during the mineral formation. To assess the influence of additives on the CaCO₃ polymorph that forms within our porous scaffolds, we add magnesium chloride (MgCl₂) to the solution used to initiate the mineralization of the capsule templates and perform X-ray diffraction (XRD) on the resulting samples. In the absence of any additive, we obtain calcite, as indicated

and-conditions) on Wiley Online Library for rules of use; OA articles are governed by the applicable Creative Commons

www.afm-journal.de

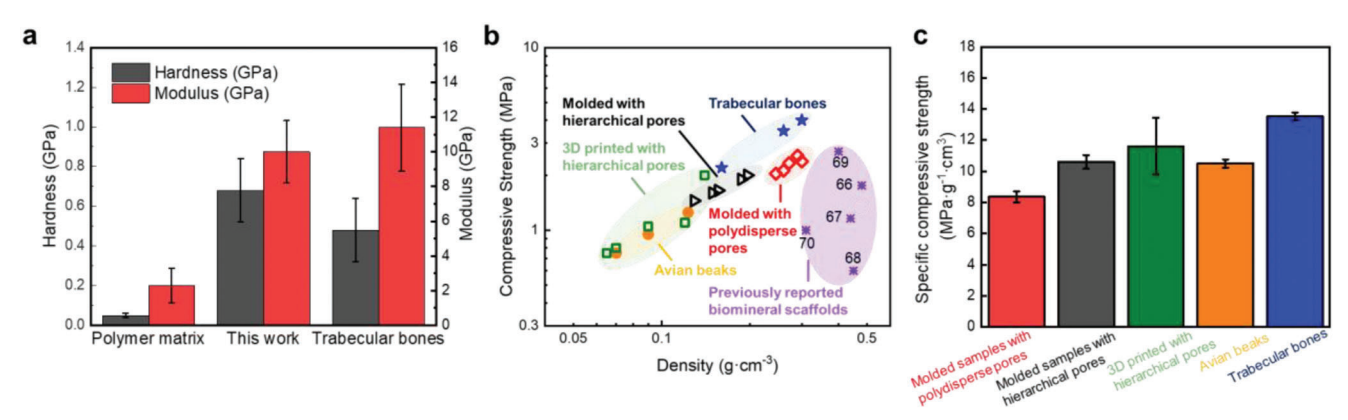


Figure 5. Mechanical behavior of 3D printed and molded porous mineral-based composites. a) Comparison of the surface hardness and stiffness of 3D printed mineralized samples, the polymer matrix and trabecular bones. [59] b) Ashby plot of the compressive strength of 3D printed (□) and molded (▷) hierarchical scaffolds made from a mixture of emulsions that have been produced through tip sonication and vortexing respectively, and molded bulk samples with polydisperse pores made from emulsions formed through vortexing solely (⋄). All the samples have been subjected to two additional mineralization cycles. The samples reported in this paper are compared to typical natural porous biominerals like avian beaks (๑), [60,61] trabecular bones (★) [62-65] and previously reported synthetic porous biominerals that possess apparent densities below 0.5 g cm⁻³. [66-70] Numbers in the charts represent relevant references. c) Specific compressive strength, defined as the compressive strength divided by the density of the material, of porous composites calculated from the compression measurements of five independent samples.

by the characteristic rhombohedral morphology of the crystals in Figure 6a,b. This result is confirmed by the synchrotron XRD trace for molded bulk samples in Figure 6e. By contrast, if mineralized in the presence of Mg²⁺, we primarily obtain aragonite, as indicated with XRD in Figure 6e and the nanograin morphology seen on SEM images in Figure 6c,d. We also get extra phases of magnesite or calcite when Mg²⁺ is not uniformly distributed in the ink formulation while trona comes from the printing bath solution when samples are not completely rinsed. If we mineralize our samples in the presence of an organic additive, polyacrylic acid (PAA), we obtain a mixture of calcite and vaterite, as demonstrated in the XRD in Figure 6e. Traditional XRD confirms these results, as shown in Figure S17 (Supporting Information). This result is consistent with results obtained by forming these minerals in bulk,^[71] suggesting that knowhow on polymorphic control of CaCO3 formation in bulk aqueous solutions can be transferred to our process.

2D scanning synchrotron XRD allows us to determine the spatial distribution of different crystal phases in printed lattice samples, as illustrated in Figure S18 (Supporting Information). In accordance with the results on bulk samples and our XRD results, a mixture of calcite and vaterite is obtained throughout the scaffold, if the mineralization is conducted in the presence of PAA, as shown in Figure 6f,g. In addition, we detect crystalline PVA from the polymer matrix and NaCl as a side product of the mineralization, as shown in Figure S19 (Supporting Information).

To assess the influence of additives on the mechanical properties, we measure the compressive strength of composites containing different CaCO₃ polymorphs. Samples formed in the presence of Mg²⁺ have a 48% higher average strength and 26% higher specific compressive strength compared to those formed in the absence of any additives, as shown in Figure S20 (Supporting Information). We assign the higher strength of the aragonite-based composites to their comparatively high inorganic content and the higher stiffness of aragonite compared to that of calcite and vaterite. [72] By contrast, samples formed in the presence of

PAA have a 14% lower average strength while possessing a similar specific strength as samples without additives.

To illustrate the potential of our material, we produce an artificial toucan bird beak with a polymeric skin and a porous mineral-based core. To achieve this goal, we cast our ink composed of upconcentrated CaCO₃-based capsules into a polymer-based beak mold. The de-molded mineral-based sample has a macroscopic shape and microscopic structure that closely resembles the interior of toucan bird beaks, as shown in **Figure 7**a. The ability to mold, inject or even 3D print these materials combined with the good biocompatibility of the components renders them well-suited scaffolds for reparation, or maybe even replacement of defective or missing natural porous minerals.^[73]

Our in situ mineralization approach offers the additional advantage that it enables firm connections between adjacent layers. such as filaments that have been sequentially deposited during a 3D printing process . For example, two individually printed grids are joined into an integral free-standing structure by bringing the two grids in contact before they are subjected to an additional mineralization cycle. The dried object is free-standing, as shown in Figure 7b, indicating that the structures are well connected. Indeed, the distribution of calcium at the interfaces is homogeneous, as revealed by Energy-dispersive X-ray (EDX) mapping. These results highlight the firm interlayer connections in our 3D printed products, which results in a high strength even if printed as multi-layer structures, as demonstrated by the SEM micrographs in Figure S21 (Supporting Information). Yet, at the end of the life of these biominerals, they can be demineralized under mildly acidic conditions using an acetate buffer. Indeed, the minerals dissolve within 4 h if put into a pH 4 acetate buffer, as shown in Figure S22 (Supporting Information). This complete dissolution of CaCO₃ renders the remaining polymer matrices reusable, depicting the sustainablity of our fabrication process.

To demonstrate the versatility of our approach, we 3D print lightweight multi-material architectures possessing locally varying compositions and pore sizes. We 3D print a butterfly whose

- Bibliothèque De L'Epf1-, Wiley Online Library on [12/09/2023]. See the Terms

) on Wiley Online Library for rules of use; OA articles are governed by the applicable Creative Commons

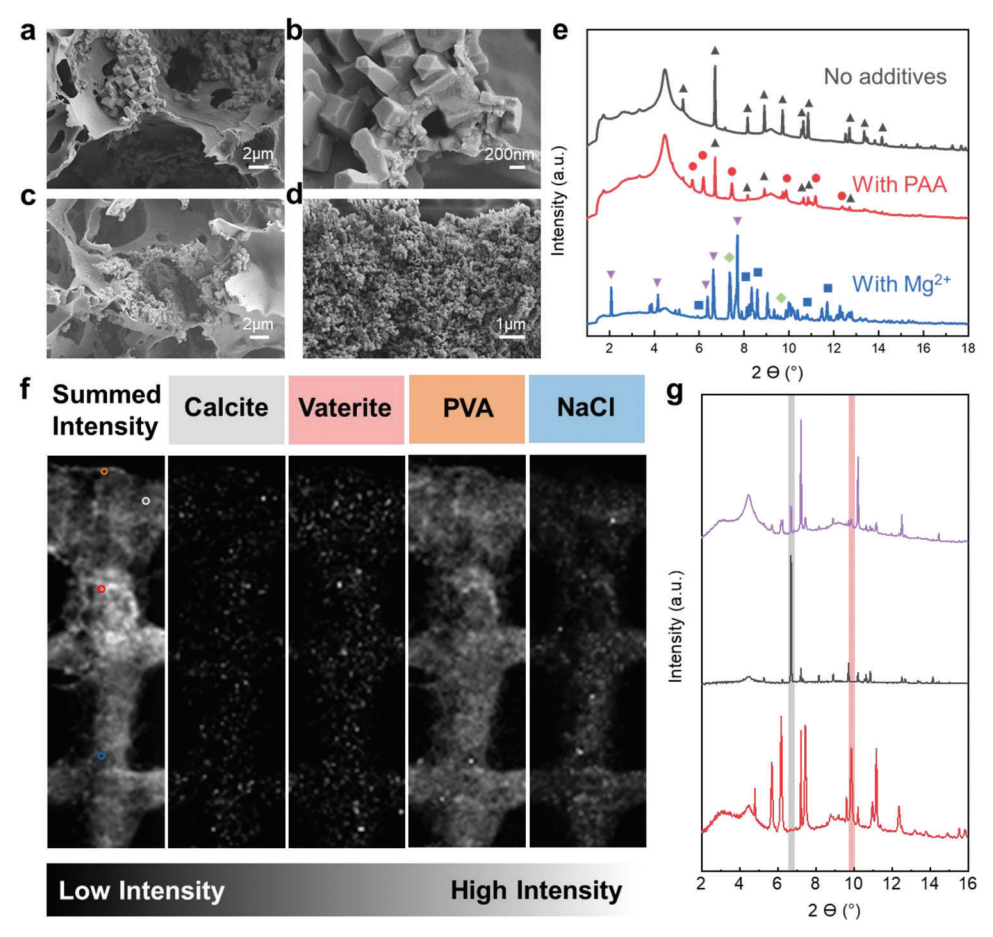


Figure 6. Mineral structures. a–d) SEM images of porous biominerals formed in the (a,b) absence of any additives and (c,d) presence of $MgCl_2$. e) Synchrotron X-ray diffraction (XRD) patterns of samples formed in the presence of Mg^{2+} (bottom), PAA (middle), and in the absence of additives (top). Detected peaks are compared to reference diffractograms of calcite (\triangle), vaterite(\bigcirc), aragonite(\bigcirc), magnesite(\bigcirc) and trona(\bigcirc). f) 2D scanning synchrotron XRD maps of a mineralized printed sample formed in the presence of PAA showing the spatial intensity distribution of the summed scattering signal as well as the diffraction peaks indicated in (g). g) Diffractograms normalized to their maximum value of the spatially averaged signal (purple) and the positions marked by gray and red circles in (f) corresponding to high amounts of calcite (black) and vaterite (red) respectively.

wings are composed of two types of inks, one that has been made by tip sonication, the other through vortexing. The two inks are co-printed into butterfly wings possessing locally varying porosities, as shown in Figure 7c and Figure S25 (Supporting Information). To leverage the ability to locally vary the composition of the 3D printed parts with a good interfacial affinity between different constituents, we co-print inks composed of capsules made of surfactants that have been crosslinked with Ca²⁺, others with Fe³⁺ and yet others that have not been crosslinked into the Na₂CO₃containing aqueous solution. SEM images and EDX mapping of the resulting heterogeneous structure demonstrate its locally varying composition, as shown in Figure 7c. Note that the microstructures of the formed Fe(OH)₃ is similar to that of CaCO₃, as shown in Figure S23 (Supporting Information). The formed $Fe(OH)_3$ can be further crystallized into hematite (α - Fe_2O_3) upon heat treatment at 800 °C for 4 h. To further demonstrate the universality of our process, we replace the carbonate source in the mineralizing solution with a phosphate source. We immerse pyrogallol functionalized capsules that have been crosslinked with Ca²⁺ into this mineralizing solution containing ammonium dihydrogen phosphate to print them into macroscopic grids. The resulting mineral is mainly composed of brushite, as verified with XRD shown in Figure S24 (Supporting Information).

3. Conclusion

We introduce a capsule-based ink that enables 3D printing of minerals possessing a hierarchical porosity with pore diameters that can be controlled from 100 nm up to the mm length scale. By tuning the mineralization conditions and porosity of the composite, we can adjust its mechanical properties to be similar to that of natural porous minerals such as human trabecular bones or the beaks of toucan birds. The tight control over the porous structure, mineral composition, and the macroscopic 3D shape is achieved through an energy-efficient process that can be performed at room temperature under aqueous conditions, thereby enabling the incorporation of thermally labile substances.

Our process starts from polymeric scaffolds that present moieties with a high affinity to Ca^{2+} , such that they can serve as active nucleation sites. In this respect, our process is similar to the natural formation of minerals albeit, in nature, the size of the individual compartments and the dimensions of the scaffolds are

- Bibliothèque De L'Epf1-, Wiley Online Library on [12/09/2023]. See the Terms

on Wiley Online Library for rules of use; OA articles are governed by the applicable Creative Common (

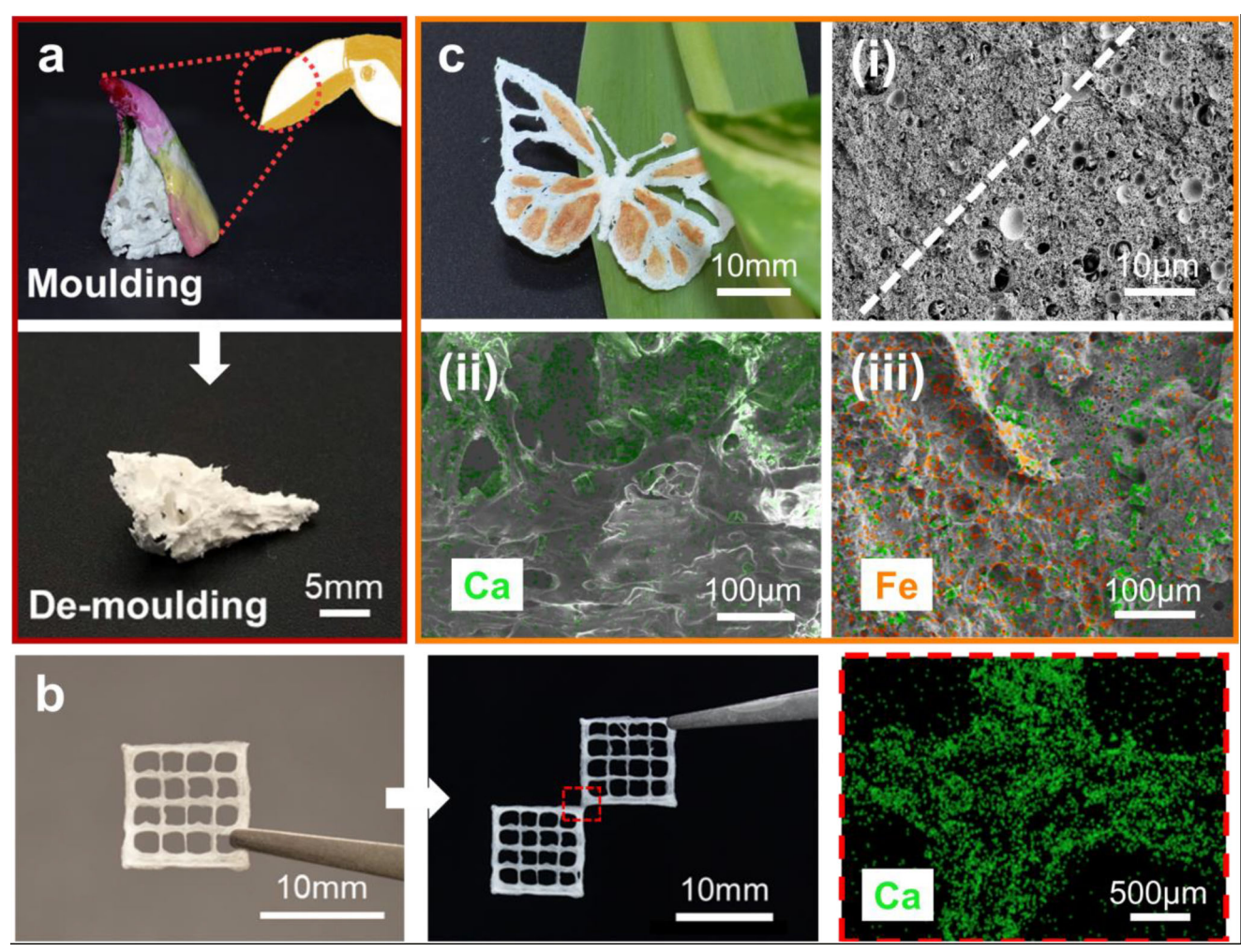


Figure 7. Proof of concept of 3D printed porous mineral-based composites. a) An artificial toucan beak made by molding inks into a 3D printed shell, exhibiting a well-defined morphology after demolding. b) Photograph of two printed mineralized lattices that have been connected through an additional mineralization cycle and corresponding EDX mapping of the connected part indicated with the red box in the middle picture. c) A 3D printed butterfly produced by co-printing different types of capsule-based inks that are sequentially mineralized. (i) SEM image of the cross-section of the printed structure demonstrating the local variations in the pore sizes. The white dashed line indicates the boundary of the two co-printed inks. EDX mapping of the butterfly surfaces revealing (ii) the gradient in the CaCO₃ concentration and (iii) the presence of Fe(OH)₃.

significantly smaller. By analogy to the natural mineralization, we subject our polymer scaffold to an aqueous environment that contains a high concentration of ions to initiate their mineralization. This procedure offers an additional advantage: through the targeted supply of additives, we can control the morphology and structure of the forming minerals, thereby offering another handle on the mechanical properties of the mineralized composites. However, albeit most of the used chemicals are biocompatible, our system cannot be used for in vivo studies as it includes fluorinated surfactants and oils. Yet, with additional work, these components can potentially be replaced with substances that are compatible with in vivo applications. In summary, we envisage the possibility to vary porosity over many orders of magnitudes coupled with the versatility of the process in terms of material selection and its energy efficiency to open up new avenues for the sustainable fabrication of the next generation of porous biominerals.

4. Experimental Section

 $\label{eq:materials: Poly(vinyl alcohol)} $(M_w \ 13000-23000, \ 87-89\% \ hydrolyzed), Trizma base (2-Amino-2-(hydroxymethyl)-1,3-propandiol), poly(acrylic acid) (average Mw 1800) and magnesium chloride hexahydrate (MgCl_2·6H_2O) were purchased from Sigma-Aldrich and used as received. Calcium chloride (CaCl_2), iron chloride (FeCl_3), and sodium carbonate (Na_2CO_3) were purchased from Carl Roth. Ammonium dihydrogen phosphate was purchased from Acros Organics. The fluorinated oil, HFE 7500 (3-ethoxy-1,1,1,2,3,4,4,5,5,6,6,6-dodecafluoro-2-trifluoromethylhexane) was purchased from 3 M Company. Acetate buffer (1 M, pH 4.0) was purchased from Thermo Scientific Chemicals. All other organic chemicals were purchased from Sigma-Aldrich.$

Production of Emulsions: An aqueous solution containing 1–10 wt% PVA and 0.1–1 M CaCl₂ was prepared and its pH was adjusted to 9 by adding Trizma base. The aqueous phase was emulsified (vortexing for 25 s) with HFE 7500 containing 2 wt% dipyrogallol-functionalized surfactant. The volume ratio between the aqueous phase and oil phase was 5:1. The resulting oil-in-water emulsions were sedimented overnight before the aqueous supernatant phase was discarded.



www.afm-journal.de

Microfluidic flow focusing devices with a channel cross-section of 100 $\mu m \times 100~\mu m$ were produced from poly(dimethylsiloxane) (PDMS) (Sylgard 184, Dow Corning) using soft lithography. The surfaces of the channels were rendered hydrophilic by injecting an aqueous solution containing 2 wt% polydiallyldimethylammonium chloride (Sigma-Aldrich) for 10 min into the channels before they were dried with compressed air. Monodisperse emulsions were made by injecting the inner oil phase at a flow rate of 30 μL min $^{-1}$ and the outer aqueous phase at a flow rate of 50 μL min $^{-1}$ using syringe pumps (Cronus Sigma 1000, Labhut).

The mixture of two batches of emulsions possessing different drop sizes was fabricated by tip sonication of the water/oil mixture with a volume ratio of 5:1 for 6 min before adding another 20 vol% oil phase containing 2 wt% surfactant and vortexing this mixture for 25 s. Both the polydisperse and monodisperse emulsions were sedimented to up-concentrate the emulsions, as described above.

Production of 3D Printed Samples: The concentrated emulsions were loaded in a 3 mL syringe. Direct ink writing-based 3D printing was performed with a commercial 3D printer (BIO X, Cellink). The capsule-based ink was extruded from a conical nozzle (515 μ m in diameter) using a pressure around 30 kPa at a printing speed of 15–20 mm s⁻¹. Printing was performed in a petri dish encompassing an aqueous solution containing 2 M Na₂CO₃. Printed structures were immersed inside the printing bath for at least 2 h.

Production of Molded Samples: The capsule-based ink was extruded into an aqueous solution containing 2 m Na $_2$ CO $_3$ to induce the gelation of PVA and initiate the mineralization. After an incubation time of 2 h, the mineralized gels were cast into molds of a cubic shape (10 mm \times 10 mm) for compression tests or beak shape for the fabrication of the artificial toucan bird beak.

Biomineralization Procedure: To reinforce samples, they were subjected to repeated mineralization cycles by incubating the printed or molded composites in an aqueous solution containing 1 $\rm M$ CaCl $_2$ for 2 h before rinsing with deionized water and again in a solution containing 1 $\rm M$ Na $_2$ CO $_3$ for 2 h respectively; this two-step mineralization is referred to as one mineralization cycle. The control over the formation of different CaCO $_3$ polymorphs during the mineralization was achieved by adding a certain amount of additives together with 0.1 $\rm M$ CaCl $_2$ to the aqueous phase used to form emulsions and to perform additional mineralization cycles. The molar ratio of Ca $^{2+}$ to PAA is 1:0.1 while the molar ratio between Ca $^{2+}$ to Mg $^{2+}$ is 1:5.

Solidification Procedure: After samples have optionally been subjected to additional mineralization cycles, they were removed from the biomineralization solution, rinsed with deionized water to remove extra salts, and dried in air at room temperature for 48 h and subsequently under vacuum for 12 h to remove all the remaining solvents.

Production of Other Biomineral Samples: To obtain iron oxide-based composites, an aqueous solution containing 5 wt% PVA and 0.1 $\,$ M FeCl $_3$ was prepared and emulsified with HFE 7500 containing 2 wt% dipyrogallol-functionalized surfactant. The obtained emulsions were concentrated and printed into an aqueous solution containing 2 M Na $_2$ CO $_3$ to perform the following hydrolysis reaction:

$$2Fe^{3+}$$
 (aq) + $3CO_3^{2-}$ (aq) + $3H_2O$ (l) $\rightarrow 2Fe(OH)_3$ (s) + $3CO_2$ (g) (1)

Fe(OH) $_3$ was crystallized into hematite (α -Fe $_2$ O $_3$) by sintering (Muffle furnace L 5/11/B410, Nabertherm) at 800 °C under air atmosphere for 4 h. To obtain calcium phosphate-based composites, an aqueous solution containing 5 wt% PVA and 0.1 m CaCl $_2$ was prepared and emulsified with HFE 7500 containing 2 wt% dipyrogallol-functionalized surfactant. The upconcentrated emulsions were printed into an aqueous solution containing 1 m ammonium dihydrogen phosphate, whose pH was adjusted to 7 by adding Trizma base to perform the following reaction:

$$Ca^{2+}$$
 (aq) + $H_2PO_4^-$ (aq) + OH^- (aq) + H_2O (l) \rightarrow $CaHPO_4 \cdot 2H_2O$ (s) (2)

Rheology of Emulsions and Mineralized Gels: Rheology was performed on a DHR-3 TA Instrument with an 8 mm diameter parallel plate steel geometry. All measurements were performed at 25 °C, with a 1000 µm

gap. Viscosity measurements were made by steady-state flow experiments with a sweep of shear rates from 0.01 to $100 \, \text{s}^{-1}$. Amplitude sweeps were performed at 1 rad s⁻¹ oscillation. Frequency sweeps were performed at a strain of 1% and an angular frequency ranging from 100 to 0.1 rad s⁻¹. Shear recovery measurements were performed at 10 rad s⁻¹, alternating 60 s at 1% strain, with 60 s at 100% strain. Samples were allowed to relax for 200 s at the set temperature before a measurement was started.

FTIR and Raman Characterization: FTIR spectra were measured on a Nicolet 6700 spectrometer (Thermo Fischer Scientific) in the attenuated total reflectance (ATR) mode, and corrected with the background signal. Traces were acquired between 4000 and 400 cm⁻¹ at a resolution of 4 cm⁻¹. Raman spectroscopy was performed on a Renishaw Raman spectrometer, equipped with a confocal microscope and a 785 nm excitation laser. The samples were dried and loaded on a glass substrate, placed under a 10× microscope lens. The laser power was 30 mW, the grating was 600 g mm⁻¹ and the energy was adjusted to 10%. The integration time was 2 s with an accumulation of 20 times.

Microstructural Analysis: The dimensions of the emulsion drops were assessed using an optical microscope (ECLIPSE TS-100, Nikon). Polarized optical microscopy images were obtained by a polarizing microscope (ECLIPSE Ti-DH, Nikon). SEM images were recorded on a Zeiss Gemini 300 operated with an accelerating voltage of 3 kV and a working distance of roughly 8 mm. Samples were coated with 10 nm of gold to avoid charging effects. EDX spectroscopy was acquired using the aforementioned Zeiss Gemini 300 equipped with an Oxford Instruments EDX detector operated at 10 kV and 180 pA beam current. The input count per second was around 3000 cps.

X-Ray Micro-Computed Tomography: The 3D morphology of printed samples was investigated by X-ray micro-computed tomography (μ-CT) using an Xradia 620 Versa X-ray microscope (ZEISS, Germany). The X-ray voltage and power were set to 40 kV and 3 W, respectively, and tomographs were acquired using a CCD camera coupled to a scintillator for X-ray-tovisible-light conversion and a 4× magnifying objective. For samples produced from varying initial concentrations of calcium as well as samples produced from monodisperse emulsions, the exposure time was adjusted to 1 s per projection to reach ≈5000 counts per pixel in the recorded projections using a detector binning of 2, and 1601 projections/360° sample rotation were recorded. This resulted in a reconstructed isotropic voxel size of 1.7 µm. For samples undergoing a varying number of mineralization cycles, the exposure time was adjusted to 8 s per projection to reach a similar count number in the recorded projections with slightly adjusted source- and detector positions and no detector binning to result in a reconstructed isotropic voxel size of 0.7 µm. For these scans, 4501 projections/360° sample rotation were recorded. 3D images were reconstructed from the projection data using the software included in the scanner. Image segmentation and visualization were performed with the Dragonfly software Version 2022.1 (Object Research Systems Inc, Montreal, Canada). Note that features below approximately twice the voxel size will not be

TGA Measurements: TGA measurements were performed with a TGA 4000 instrument (PerkinElmer). For each measurement, dry samples with the weight of 10–50 mg were placed into crucibles and heated from 30 °C to 900 °C at a rate of 10 °C min $^{-1}$ under a flow of dry air with a flow rate of 20 mL min $^{-1}$. Measurements were repeated at least three times for each type of samples and reported as mean \pm standard deviation.

XRD Measurement: XRD patterns were acquired using an Empyrean diffractometer (Malvern Panalytical) with 2θ ranging from 20° to 60° , at a scanning rate of 0.1° s⁻¹. The radiation source was Cu K α with a wavelength of 1.5405 Å and the generator was operated at 40 keV, 40 mA. All samples were finely ground before testing.

4.0.0.1. Scanning Synchrotron XRD: The spatial distribution of crystallographic phases was investigated in selected samples by 2D scanning XRD performed at the DANMAX beamline of the MAX IV synchrotron (Sweden). The X-ray beam was adjusted to 35 keV (corresponding to a wavelength of 0.354 Å) using a Si (111) horizontal double crystal monochromator combined with a horizontal double multilayer monochromator and focused to $10 \times 20~\mu\text{m}^2$ using beryllium compound refractive lenses (Be CRLs). The samples were mounted on Kapton tape on a



www.afm-journal.de

translation stage and selected ROIs were raster scanned through the beam. Scattering patterns were collected for every 30 µm translational step on a PILATUS3×2 M detector (DECTRIS AG, Switzerland) placed 518 mm from the sample with an exposure time of 1 s. The resulting 2D scattering patterns were azimuthally integrated using MatFRAIA^[75] in MATLAB version R2021B (MathWorks, MA, USA) to give one 1D diffractogram for each sample position. For molded (bulk) samples, these were averaged to give a single high S/N-diffractogram that was compared to reference diffractograms of relevant crystal phases for phase identification. For printed (lattice) samples, diffraction data stemming from air/Kapton was subtracted from the position-resolved data prior to further processing. A reflection with unique 2θ was selected for each identified crystal phase: the (101) reflection for crystalline PVA ($2\theta = 3.91-4.99^{\circ}$), the (104) reflection for calcite ($2\theta = 6.61 - 6.78^{\circ}$), the ($2\bar{1}8$) reflection for vaterite ($2\theta = 9.76 - 9.94^{\circ}$), and the (200) reflection for NaCl ($2\theta = 7.11-7.31^{\circ}$). The intensity of each of these reflections, subtracted a local background and normalized to its maximum value within the given ROI, was plotted as a function of sample position to visualize the spatial distribution of the corresponding phase. Furthermore, a plot of the total (summed) scattering intensity was plotted as a function of position to serve as a reference image of the sample.

Nanoindentation: Nanoindentation measurements were conducted on an Anton Paar NHT3 tester mounted with a Berkovich indenter. The experiment was performed in a displacement control mode with a maximum indentation depth of 5000 nm and a displacement rate of 1000 nm min⁻¹. Before the drying was complete, the samples were placed into a steel mold. The following pre-press procedure was executed using the Programmable Hydraulic Pellet Press machine (PIKE Technologies): Within the first 5 min, the pressure applied to the sample was gradually increased from 0 to 20 MPa. Then a constant pressure of 200 MPa was applied for 30 min. After pressing, the samples were dried in a vacuum chamber and polished with sand papers before indentation tests were performed to obtain flat and smooth surfaces

Compression Tests: Compressive strength measurements were performed with a commercial uniaxial testing machine (ZwickiLine 5 kN, Zwick Roell) equipped with a 100 N load cell. Samples were molded into cubic shapes with the size of 10 mm \times 10 mm \times 10 mm or printed into lattices with the size of 10 mm \times 10 mm \times 5 mm. Compression tests were conducted in the displacement control mode at a rate of 1 mm min $^{-1}$ until samples broke or a strain of 90% was reached. Note that densities listed in this work were apparent densities obtained from weight and volume measurements. The densities of previously reported synthetic porous biominerals were calculated by the following equation:

$$\rho_{A} = \rho_{B} \ (100 \% - P) \tag{3}$$

where ρ_A is the apparent density of scaffolds, ρ_B is the bulk density of components contained in the materials and P is the porosity in percentage.

Supporting Information

Supporting Information is available from the Wiley Online Library or from the author.

Acknowledgements

The authors thank Dr. Alvaro Charlet for the help with Raman spectroscopy, and Yutong Peng for the assistance in doing rheology and 3D printing tests. The authors acknowledge David Wen Hua Bi for the help with the XRD experiments and data analysis, Thorbjørn Erik Køppen Christensen for performing the MatFRAIA integration of the synchrotron XRD data, and Yann Lavanchy for his help with the TGA analysis. Use of the Novo Nordisk Foundation research infrastructure AXIA (grant NNF19OC0055801) is acknowledged. Additionally, the authors acknowledge the MAX IV Laboratory for time on the DanMAX beamline under proposal 20210507 as well as beamline staff, especially Dr. Mads Ry Vogel Jørgensen, for assistance during the beamtime. Research conducted

at MAX IV is supported by the Swedish Research Council under contract 2018-07152, the Swedish Governmental Agency for Innovation Systems under contract 2018-04969, and Formas under contract 2019-02496. Dan-MAX is funded by the NUFI grant no. 4059-00009B. The work was financially supported by the Swiss National Competence in Research (NCCR) Bio-inspired Materials (205603).

Open access funding provided by Ecole Polytechnique Federale de Lausanne

Conflict of Interest

The authors declare no conflict of interest.

Author Contributions

R.Z. and E.A. designed and coordinated the study. R.Z. performed the experiments. N.K.W., supervised by H.B., carried out the X-ray $\mu\text{-CT}$ and synchrotron XRD characterization. These data were analyzed by N.K.W. and H.B. G.D.A. and T.Y. synthesized the surfactants. R.Z., N.K.W., and E.A. prepared the manuscript. All authors discussed the results and reviewed on the manuscript.

Data Availability Statement

The data that support the findings of this study are available from the corresponding author upon reasonable request.

Keywords

3D printing, CaCO₃, emulsion templating, porous biominerals

Received: January 26, 2023 Revised: May 9, 2023 Published online:

- J. Aizenberg, J. C. Weaver, M. S. Thanawala, V. C. Sundar, D. E. Morse, P. Fratzl, Science 2005, 309, 275.
- [2] T. Yang, H. Chen, Z. Jia, Z. Deng, L. Chen, E. M. Peterman, J. C. Weaver, L. Li, *Science* 2022, 375, 647.
- [3] P.-Y. Chen, J. McKittrick, M. A. Meyers, Prog. Mater. Sci. 2012, 57, 1492.
- [4] U. G. K. Wegst, H. Bai, E. Saiz, A. P. Tomsia, R. O. Ritchie, *Nat. Mater.* 2015, 14, 23.
- [5] P. Fratzl, O. Kolednik, F. D. Fischer, M. N. Dean, Chem. Soc. Rev. 2016, 45, 252.
- [6] M. Eder, S. Amini, P. Fratzl, Science 2018, 362, 543.
- [7] D. G. Moore, L. Barbera, K. Masania, A. R. Studart, *Nat. Mater.* 2020, 19, 212.
- [8] Z. Dong, H. Cui, H. Zhang, F. Wang, X. Zhan, F. Mayer, B. Nestler, M. Wegener, P. A. Levkin, Nat. Commun. 2021, 12, 247.
- [9] F. Bouville, E. Maire, S. Meille, B. Van de Moortèle, A. J. Stevenson, S. Deville, Nat. Mater. 2014, 13, 508.
- [10] Z. Xu, M. Wu, W. Gao, H. Bai, Sci. Adv. 2022, 8, eabo0946.
- [11] H. L.e Ferrand, F. Bouville, T. P. Niebel, A. R. Studart, *Nat. Mater.* 2015, 14, 1172.
- [12] A. Amini, A. Khavari, F. Barthelat, A. J. Ehrlicher, Science 2021, 373, 1229
- [13] Y. Yang, X. Li, M. Chu, H. Sun, J. Jin, K. Yu, Q. Wang, Q. Zhou, Y. Chen, Sci. Adv. 2019, 5, eaau9490.



www.afm-journal.de

- [14] M. A. Meyers, J. McKittrick, P.-Y. Chen, Science 2013, 339, 773.
- [15] Y. Wang, S. E. Naleway, B. Wang, Bioact. Mater. 2020, 5, 745.
- [16] J. Song, V. Malathong, C. R. Bertozzi, J. Am. Chem. Soc. 2005, 127, 3366.
- [17] H. Ping, W. Wagermaier, N. Horbelt, E. Scoppola, C. Li, P. Werner, Z. Fu, P. Fratzl, Science 2022, 376, 188.
- [18] T. Kato, Adv. Mater. 2000, 12, 1543.
- [19] C. Xiao, M. Li, B. Wang, M.-F. Liu, C. Shao, H. Pan, Y. Lu, B.-B. Xu, S. Li, D. Zhan, Y. Jiang, R. Tang, X. Y. Liu, H. Cölfen, *Nat. Commun.* 2017. 8, 1398.
- [20] W. Chen, P. Zhang, R. Zang, J. Fan, S. Wang, B. Wang, J. Meng, Adv. Mater. 2020, 32, 1907413.
- [21] L.-B. Mao, H.-L. Gao, H.-B. Yao, L. Liu, H. Colfen, G. Liu, S.-M. Chen, S.-K. Li, Y.-X. Yan, Y.-Y. Liu, S.-H. Yu, Science 2016, 354, 107.
- [22] A. Xin, Y. Su, S. Feng, M. Yan, K. Yu, Z. Feng, K. H. Lee, L. Sun, Q. Wang, Adv. Mater. 2021, 33, 2006946.
- [23] L.-B. Mao, Y.-F. Meng, X.-S. Meng, B. Yang, Y.-L. Yang, Y.-J. Lu, Z.-Y. Yang, L.-M. Shang, S.-H. Yu, J. Am. Chem. Soc. 2022, 144, 18184.
- [24] Z. C. Eckel, C. Zhou, J. H. Martin, A. J. Jacobsen, W. B. Carter, T. A. Schaedler, *Science* 2016, 351, 58.
- [25] A. Imhof, D. J. Pine, Nature 1997, 389, 948.
- [26] I. Akartuna, A. R. Studart, E. Tervoort, L. J. Gauckler, Adv. Mater. 2008, 20, 4714.
- [27] C. Minas, D. Carnelli, E. Tervoort, A. R. Studart, Adv. Mater. 2016, 28, 9993.
- [28] F. Zhang, Z. Li, M. Xu, S. Wang, N. Li, J. Yang, J. Eur. Ceram. Soc. 2022, 42, 3351.
- [29] S. Romanazzo, T. G. Molley, S. Nemec, K. Lin, R. Sheikh, J. J. Gooding, B. Wan, Q. Li, K. A. Kilian, I. Roohani, Adv. Funct. Mater. 2021, 31, 2008216.
- [30] J. T. Muth, P. G. Dixon, L. Woish, L. J. Gibson, J. A. Lewis, Proc. Natl. Acad. Sci. USA 2017, 114, 1832.
- [31] H. P. Voisin, K. Gordeyeva, G. Siqueira, M. K. Hausmann, A. R. Studart, L. Bergström, ACS Sustainable Chem. Eng. 2018, 6, 17160.
- [32] Q. Fu, E. Saiz, A. P. Tomsia, Adv. Funct. Mater. 2011, 21, 1058.
- [33] B. Román-Manso, J. Muth, L. J. Gibson, W. Ruettinger, J. A. Lewis, ACS Appl. Mater. Interfaces 2021, 13, 8976.
- [34] J. Guo, Y. Ping, H. Ejima, K. Alt, M. Meissner, J. J. Richardson, Y. Yan, K. Peter, D. von Elverfeldt, C. E. Hagemeyer, F. Caruso, Angew. Chem., Int. Ed. 2014, 53, 5546.
- [35] A. Andersen, M. Krogsgaard, H. Birkedal, Biomacromolecules 2018, 19, 1402.
- [36] M. Krogsgaard, A. Andersen, H. Birkedal, Chem. Commun. 2014, 50, 13278.
- [37] R. Lakes, Nature 1993, 361, 511.
- [38] G. Etienne, I. L. H. Ong, E. Amstad, Adv. Mater. 2019, 31, 1808233.
- [39] G. De Angelis, N. Grey, V. Lutz-Bueno, E. Amstad, Adv. Mater. Interfaces 2023, 10, 2202450.
- [40] A. C. Daly, L. Riley, T. Segura, J. A. Burdick, Nat. Rev. Mater. 2020, 5, 20
- [41] M. J. Harrington, A. Masic, N. Holten-Andersen, J. H. Waite, P. Fratzl, Science 2010, 328, 216.
- [42] S. Wu, M. Hua, Y. Alsaid, Y. Du, Y. Ma, Y. Zhao, C.-Y. Lo, C. Wang, D. Wu, B. Yao, J. Strzalka, H. Zhou, X. Zhu, X. He, Adv. Mater. 2021, 33, 2007829.
- [43] M. Hua, S. Wu, Y. Ma, Y. Zhao, Z. Chen, I. Frenkel, J. Strzalka, H. Zhou, X. Zhu, X. He, *Nature* 2021, 590, 594.
- [44] A. Charlet, V. Lutz-Bueno, R. Mezzenga, E. Amstad, Nanoscale 2021, 13, 4073.

- [45] N. Hosoda, A. Sugawara, T. Kato, Macromolecules 2003, 36, 6449.
- [46] Q. Li, D. G. Barrett, P. B. Messersmith, N. Holten-Andersen, ACS Nano 2016, 10, 1317.
- [47] S. Kim, A. U. Regitsky, J. Song, J. Ilavsky, G. H. McKinley, N. Holten-Andersen, Nat. Commun. 2021, 12, 667.
- [48] H. Jodati, B. Yılmaz, Z. Evis, Ceram. Int. 2020, 46, 15725.
- [49] M. Sari, P. Hening, Chotimah, I. D. A., Y. Yusuf, Biomater. Res. 2021, 25. 2.
- [50] X. Zheng, H. Lee, T. H. Weisgraber, M. Shusteff, J. DeOtte, E. B. Duoss, J. D. Kuntz, M. M. Biener, Q. Ge, J. A. Jackson, S. O. Kucheyev, N. X. Fang, C. M. Spadaccini, *Science* 2014, 344, 1373.
- [51] W. Huo, X. Zhang, E. Tervoort, S. Gantenbein, J. Yang, A. R. Studart, Adv. Funct. Mater. 2020, 30, 2003550.
- [52] Y. Seki, M. S. Schneider, M. A. Meyers, Acta Mater. 2005, 53, 5281.
- [53] F. Monchau, Ph. Hivart, B. Genestie, F. Chai, M. Descamps, H. F. Hildebrand, Mater. Sci. Eng. C 2013, 33, 490.
- [54] L. J. Gibson, M. F. Ashby, Cellular Solids: Structure and Properties, 2nd ed., Cambridge University Press, Cambridge 1997.
- [55] U. G. K. Wegst, M. F. Ashby, Philos. Mag. 2004, 84, 2167.
- [56] T. N. Sullivan, B. Wang, H. D. Espinosa, M. A. Meyers, *Mater. Today* 2017, 20, 377.
- [57] C. Merkel, J. Deuschle, E. Griesshaber, S. Enders, E. Steinhauser, R. Hochleitner, U. Brand, W. W. Schmahl, J. Struct. Biol. 2009, 168, 407.
- [58] T. Yang, Z. Jia, H. Chen, Z. Deng, W. Liu, L. Chen, L. Li, Proc. Natl. Acad. Sci. USA 2020, 117, 23450.
- [59] P. K. Zysset, X. E. Guo, C. E. Hoffler, K. E. Moore, S. A. Goldstein, Technol. Health Care 1998, 6, 429.
- [60] Y. Seki, S. G. Bodde, M. A. Meyers, Acta Biomater. 2010, 6, 331.
- [61] Y. Seki, B. Kad, D. Benson, M. A. Meyers, Mater. Sci. Eng. C 2006, 26, 1412.
- [62] L. Røhl, E. Larsen, F. Linde, A. Odgaard, J. Jørgensen, J. Biomech. 1991, 24, 1143.
- [63] J.-T. Hsu, H.-L. Huang, C.-H. Chang, M.-T. Tsai, W.-C. Hung, L.-J. Fuh, Int. J. Oral Maxillofac. Implants 2013, 28, 367.
- [64] R. Oftadeh, M. Perez-Viloria, J. Villa-Camacho, A. Vaziri, A. Nazarian, J. Biomech. Eng. 2015, 137, 0108021.
- [65] C. Öhman-Mägi, O. Holub, D. Wu, R. M. Hall, C. Persson, JOR Spine 2021, 4, e1176.
- [66] L. A. Cyster, D. M. Grant, S. M. Howdle, F. R. A. J. Rose, D. J. Irvine, D. Freeman, C. A. Scotchford, K. M. Shakesheff, *Biomaterials* 2005, 26, 697.
- [67] J. Wu, C. Ruan, Y. Ma, Y. Wang, Y. Luo, J. Mater. Sci. Technol. 2018, 34, 503.
- [68] M. Mbarki, P. Sharrock, M. Fiallo, H. ElFeki, Mater. Sci. Eng. C 2017, 76, 985
- [69] F. J. Martínez-Vázquez, M. V. Cabañas, J. L. Paris, D. Lozano, M. Vallet-Regí, Acta Biomater. 2015, 15, 200.
- [70] M. Potoczek, A. Zima, Z. Paszkiewicz, A. Ślósarczyk, *Ceram. Int.* 2009, 35, 2249.
- [71] S. Zhang, O. Nahi, L. Chen, Z. Aslam, N. Kapur, Y.-Y. Kim, F. C. Meldrum, Adv. Funct. Mater. 2022, 32, 2201394.
- [72] O. P. Troncoso, F. G. Torres, J. Arroyo, K. N. Gonzales, M. Fernández-García, D. López, Bioinspired, Biomimetic Nanobiomater. 2020, 9, 112.
- [73] D. de M. Pereira, P. Habibovic, Adv. Healthcare Mater. 2018, 7, 1800700.
- [74] Y. Xia, G. M. Whitesides, Angew. Chem., Int. Ed. 1998, 37, 550.
- [75] A. B. Jensen, T. E. K. Christensen, C. Weninger, H. Birkedal, J. Synchrotron Radiat. 2022, 29, 1329.